Reconstruction of conductivity using the dual-loop method with one injection current in MREIT

2010 Phys. Med. Biol. 55 7523

(http://iopscience.iop.org/0031-9155/55/24/009)

IOP PUBLISHING PHYSICS IN MEDICINE AND BIOLOGY

Phys. Med. Biol. **55** (2010) 7523–7539 doi:10.1088/0031-9155/55/24/009

Reconstruction of conductivity using the dual-loop method with one injection current in MREIT

Tae Hwi Lee[1], Hyun Soo Nam[2], Min Gi Lee[3], Yong Jung Kim[3], Eung Je Woo[1] and Oh In Kwon[2]

[1] Department of Biomedical Engineering, Kyung Hee University, Seoul, Korea
[2] Department of Mathematics, Konkuk University, Seoul, Korea
[3] Department of Mathematical Sciences, KAIST, Daejeon, Korea

E-mail: oikwon@konkuk.ac.kr

Received 12 May 2010, in final form 20 September 2010
Published 19 November 2010
Online at stacks.iop.org/PMB/55/7523

Abstract

Magnetic resonance electrical impedance tomography (MREIT) is to visualize the internal current density and conductivity of an electrically conductive object. Injecting current through surface electrodes, we measure one component of the induced internal magnetic flux density using an MRI scanner. In order to reconstruct the conductivity distribution inside the imaging object, most algorithms in MREIT have required multiple magnetic flux density data by injecting at least two independent currents. In this paper, we propose a direct method to reconstruct the internal isotropic conductivity with one component of magnetic flux density data by injecting one current into the imaging object through a single pair of surface electrodes. Firstly, the proposed method reconstructs a projected current density which is a uniquely determined current from the measured one-component magnetic flux density. Using a relation between voltage potential and current, based on Kirchhoff's voltage law, the proposed method is designed to use a combination of two loops around each pixel from which to derive an implicit matrix system for determination of the internal conductivity. Results from numerical simulations demonstrate that the proposed algorithm stably determines the conductivity distribution in an imaging slice. We compare the reconstructed internal conductivity distribution using the proposed method with that using a conventional method with agarose gel phantom experiments.

(Some figures in this article are in colour only in the electronic version)

1. Introduction

Using a magnetic resonance imaging (MRI) scanner, magnetic resonance electrical impedance tomography (MREIT) utilizes measured magnetic flux density data by injected currents in order to visualize the conductivity and/or current density distributions inside an imaging object. The

internal current density distribution has been studied in magnetic resonance current density imaging (MRCDI) by measuring the whole magnetic flux density data $\mathbf{B} = (B_x, B_y, B_z)$ (Joy *et al* 1989, Scott *et al* 1991).

In an earlier stage of MREIT, assuming that the internal current $\mathbf{J} = (J_x, J_y, J_z)$ is available by rotations of the imaging object in an MR scanner, several conductivity image reconstruction algorithms were developed using one or two injection currents such as the J-substitution algorithm (Kwon *et al* 2002a), current-constrained voltage-scaled reconstruction algorithm (Birgul *et al* 2003) and equipotential line methods (Kwon *et al* 2002b, Ider *et al* 2003, Lee 2004).

Since an MRI scanner measures only one component B_z of $\mathbf{B}$ without rotating the imaging object, most algorithms for MREIT assume that the conductivity is isotropic and focus on visualizing its distribution by using one component of the magnetic flux density data (Ider and Birgul 1998, Kwon *et al* 2002a, Lee *et al* 2003, Oh *et al* 2003, 2004, 2005, Seo *et al* 2003, Muftuler *et al* 2004, Ider and Onart 2004, Gao *et al* 2006, Hamamura *et al* 2006, Birgul *et al* 2006).

Since there exist infinitely many isotropic conductivity distributions which generate the same magnetic flux density B_z (Kim *et al* 2003) without any additional information, most algorithms to reconstruct the isotropic conductivity image using the relation between the measured B_z data and the conductivity require at least two injection currents and measure the corresponding B_z data.

Recently, imaging techniques in MREIT have been developed with regard to the capacity of measurement techniques, as well as numerical reconstruction algorithms. Experimental results have been reported using animals and the human leg (Kim *et al* 2008, 2009). For more practical approaches, reduction in the acquisition time of scanning has become critical to *in vivo* implementation of MREIT. Since experimental MREIT techniques have included interleaved phase-encoding acquisition, two currents with positive and negative polarities, and with the same duration and amplitude for distinguishing the accumulated phase signal yield doubling of acquisition time. Moreover, most algorithms for reconstruction of the internal conductivity distribution require relatively long scanning time because they use plural magnetic flux density B_z data by independently injected currents.

Although at least two orthogonally injected currents are definitely beneficial in order to determine the internal conductivity by compensating each other, for some practical applications for MREIT, information extraction of conductivity using one injection current is important and provides a meaningful potential in the studies of the human body. Electrical brain stimulation (EBS) as a technique used in clinical neurobiology in the brain using an electric current includes deep brain stimulation (DBS) which is a neurosurgical treatment stimulating the brain by injecting current (Kringelbach *et al* 2007), cranial electrotherapy stimulation (CES) for anxiety, depression and drug addiction, transcranial direct current stimulation (tDCS) to modulate the activity of neurons in the brain by injecting electrical currents (Cogiamanian *et al* 2008), etc. Another important feasible application is functional MREIT, as a technique to image brain activity via conductivity change related to neural activity in a short total scan time.

Since the biological tissues, particularly skeletal muscle and brain white matter, have anisotropy due to asymmetric cellular structures, it will be important to extract anisotropic electrical property corresponding to each component of current flow.

In this paper, we propose a method to reconstruct an isotropic conductivity image using only one injection current and the corresponding measured B_z data under some feasible conditions. One is that the difference $J_z - J_z^0$ is small, where J_z is the z-component of the internal current caused by the injection current and J_z^0 is the z-component of the generated

current when the internal conductivity is homogeneous. From the measured B_z data, we recover a projected current density $\mathbf{J}^P$ directly by solving a two-dimensional harmonic equation, which provides a good approximation to the true current $\mathbf{J}$ stably depending on the difference $J_z - J_z^0$ (Park *et al* 2007). For practical implementations, a transversally injected current through the attached electrodes possibly reduces the difference $J_z - J_z^0$ and maximizes the measured B_z signal by the Biot–Savart law. The other is the use of reference conductivity values given in a part of the surface. Recent human imaging experiments in MREIT use a carbon-hydrogel electrode covering large surface area with a known conductivity value to inject current as much as possible without producing a painful sensation and motion artifact (Kim *et al* 2009). For the human leg experiment in Kim *et al* (2009), the sizes of the carbon electrode and hydrogel are $80 \times 60 \times 0.06$ mm^3 and $80 \times 60 \times 5.7$ mm^3, respectively.

Using the projected current instead of the true internal current, we can focus on the development of an algorithm for reconstruction of the internal conductivity distribution using the relation between the conductivity and the current. For a given internal current, a key observation is to relate the internal conductivity directly to the internal current and the unknown internal voltage u by using Kirchhoff's voltage law, $0 = \int_D \nabla \times \nabla u(\mathbf{r})\, d\mathbf{r} = \int_{\partial D} u\, d\ell$, where D is an arbitrary region. By taking each pixel as a region D and starting from a pixel with the known conductivity, we can directly recover the conductivity pixel-by-pixel by using a previously solved conductivity and combining with Kirchhoff's voltage law following the boundary of D. This one-loop method directly recovers the conductivity in a real time with a partial information of conductivity, but it heavily depends on an evolving path and easily propagates the noise effect along the evolving path. To overcome these difficulties, we design another loop which has a common intersection with the loop of the one-loop method. The designed dual-loop method produces an implicit overdetermined matrix system for the internal conductivity distribution, which is independent of any pathway and stably determines the internal conductivity directly using the measured B_z data by one injection current.

The proposed method is demonstrated with numerical simulations and phantom experiments. In phantom experiments, we used the ICNE MR pulse sequence (Park *et al* 2007) which injects current up to the data acquisition time to reduce the noise level of measured B_z data. We reconstructed and compared the interior conductivity distributions of an agarose gel phantom using both one injection current and two injection currents. The recovered conductivity image shows the feasibility of the proposed algorithm.

2. Method

We inject a current I through attached electrodes on a three-dimensional conducting object Ω. The injection current I produces a voltage distribution u satisfying the following elliptic partial differential equation:

$$\begin{aligned} &\nabla \cdot (\sigma \nabla u) = 0 \qquad \text{in} \quad \Omega \\ &-\sigma \nabla u \cdot \mathbf{n} = g \qquad \text{on} \quad \partial\Omega \qquad \text{and} \qquad \int_{\partial\Omega} u\, ds = 0, \end{aligned} \tag{1}$$

where $\mathbf{n} = (n_1, n_2, n_3)$ is the outward unit-normal vector on $\partial\Omega$ and g is the current density on $\partial\Omega$ by the injection current I. The internal current density $\mathbf{J} = -\sigma\nabla u$ and the magnetic flux density $\mathbf{B} = (B_x, B_y, B_z)$ in Ω satisfy the Ampere law $\mathbf{J} = \nabla \times \mathbf{B}/\mu_0$ where μ_0 is the magnetic permeability of the free space.

The imaging domain Ω can be expressed as the union of slices which are perpendicular to the z-axis:

$$\Omega = \bigcup_{t \in (-H, H)} \Omega_t, \qquad \text{where} \quad \Omega_t = \Omega \cap \{(x, y, z) \in \mathbb{R}^3 | z = t\}. \tag{2}$$

In the paper Park *et al* (2007), the only recoverable current is $\mathbf{J}^P = \mathbf{J}^0 + \mathbf{J}^*$ from the measured B_z data, where $\mathbf{J}^0 = \nabla\alpha$ and $\mathbf{J}^* = \left(\frac{\partial\beta}{\partial y}, -\frac{\partial\beta}{\partial x}, 0\right)$. Here α is a homogeneous voltage potential satisfying

$$\begin{aligned} &\nabla^2\alpha = 0 \qquad \text{in} \quad \Omega \\ &\nabla\alpha\cdot\mathbf{n} = \mathbf{J}\cdot\mathbf{n} \qquad \text{on} \quad \partial\Omega \qquad \text{and} \quad \int_{\partial\Omega}\alpha\,\mathrm{d}s = 0, \end{aligned} \tag{3}$$

and $\beta_t(x, y) := \beta(x, y, t)$ satisfies the following two-dimensional Laplace equation for each slice $\Omega_t \subset \Omega$:

$$\begin{aligned} &\tilde{\nabla}^2\beta_t = \frac{1}{\mu_0}\nabla^2 B_z \qquad \text{in} \quad \Omega_t \\ &\beta_t = 0 \qquad \text{on} \quad \partial\Omega_t, \end{aligned} \tag{4}$$

where $\nabla = \left(\frac{\partial}{\partial x}, \frac{\partial}{\partial y}, \frac{\partial}{\partial z}\right)$ and $\tilde{\nabla} = \left(\frac{\partial}{\partial x}, \frac{\partial}{\partial y}\right)$. Equations (3) and (4) show that we can reconstruct the projected current $\mathbf{J}^P$ from measured B_z immediately by solving two-dimensional Laplace equations in the region of interest (ROI). The projected current $\mathbf{J}^P$ provides an optimal approximation of the true current $\mathbf{J}$, and the gap $\mathbf{J} - \mathbf{J}^P$ depends only on the longitudinal component $J_z - J_z^0$ of $\mathbf{J} - \mathbf{J}^0$.

2.1. Relation between conductivity and current $\mathbf{J} = -\sigma\nabla u$

To observe the relation between the discontinuous conductivity and the current flow, we assume that $\mathbf{J}(\mathbf{r}) = (J_x(\mathbf{r}), J_y(\mathbf{r}), 0)$ in $\Omega = \bigcup_{t\in(-H,H)}\Omega_t$, and σ belongs to the following class:

$$\begin{aligned} \Sigma_t := \Bigg\{ \sigma = \sigma_0 + \sum_{k=1}^{M}\sigma_k\chi_{D_k} \Bigg| \bar{D}_k \subset \Omega_t,\ \bar{D}_k \cap \bar{D}_\ell = \emptyset \ \text{for}\ k \neq \ell, \\ \sigma_k \text{ is smooth in } D_k \text{ and } \partial D_k \text{ is smooth} \Bigg\}, \end{aligned} \tag{5}$$

where χ_{D_k} denotes the characteristic function for D_k. For a given current g and $\sigma \in \Sigma_t$, the theory of the elliptic partial differential equation (Gilbarg and Trudinger 1983) leads to

$$\begin{aligned} &\sigma_0(\xi)\nabla u^+(\xi)\cdot\mathbf{n}(\xi) = (\sigma_0(\xi) + \sigma_k(\xi))\nabla u^-(\xi)\cdot\mathbf{n}(\xi) \qquad \text{if} \quad \xi \in \partial D_k \\ &\nabla u^+(\xi)\cdot\tau(\xi) = \nabla u^-(\xi)\cdot\tau(\xi) \qquad \text{if} \quad \xi \in \partial D_k, \end{aligned} \tag{6}$$

where τ is the unit tangent vector to ∂D_k and $u^\pm$ are

$$u^+ = u|_{\Omega_t\setminus\bigcup_{k=1}^M \bar{D}_k} \qquad \text{and} \qquad u^- = u|_{\bigcup_{k=1}^M D_k}.$$

The interior current flow $\mathbf{J}$ can be decomposed as

$$\mathbf{J}(\xi) = (\mathbf{J}(\xi)\cdot\mathbf{n}(\xi))\mathbf{n}(\xi) + (\mathbf{J}(\xi)\cdot\tau(\xi))\tau(\xi) \qquad \text{for} \quad \xi \in \partial D_k. \tag{7}$$

Using (6) and (7), for $\xi \in \partial D_k$, we have

$$\begin{aligned} \mathbf{J}^-(\xi) - \mathbf{J}^+(\xi) &= (\mathbf{J}^-(\xi)\cdot\tau(\xi) - \mathbf{J}^+(\xi)\cdot\tau(\xi))\tau(\xi) \\ &= (\sigma_k(\xi)\nabla u^-(\xi))\cdot\tau(\xi)\tau(\xi). \end{aligned} \tag{8}$$

Relations (6) and (8) imply that it is difficult to distinguish the edge of anomaly near the region using the relation between the conductivity and the current, where the current flow $\mathbf{J}$ is almost orthogonal to the tangential vector τ on ∂D_k. In fact, with the motivation by the observation (8) without any assumption on the conductivity, there are infinitely many isotropic conductivity distributions which generate the same current $\mathbf{J}$ in Ω (Kim *et al* 2003) even

when $\mathbf{J}$ is a two-dimensional current. For these reasons, most of developed algorithms for conductivity reconstruction in MREIT, using the relation between the internal conductivity and the current density flow, evidently require at least two independent injection currents I^i, $i = 1, \ldots, N$, to distinguish discontinuous conductivity.

Further observations on the relationships between the conductivity and the measured B_z data, under the assumptions that a two-dimensional current $\mathbf{J} = -\sigma \nabla u = -\left(\sigma \frac{\partial u}{\partial x}, \sigma \frac{\partial u}{\partial y}, 0\right)$ is non-vanishing in Ω and the conductivity value on $\partial\Omega$ is known, guarantee that the measured B_z with current injected in one dimension uniquely determines the interior conductivity σ in Ω (Park *et al* 2007). The requirement for the use of at least two independent injection currents to visualize the interior is due to the distinguishability of the conductivity rather than the unique determination of the conductivity.

For the conductivity values on the surface, recent advancements in MREIT have used the carbon-hydrogel electrode (HUREV Co. Ltd, Korea), which covers a large part of the surface with known conductivity values 2.86×10^4 and 0.17 S m^{-1}, respectively. The large size of these electrodes enables a wide coverage of the object to induce a more uniform current density distribution inside the imaging region, and provides conductivity values around the surface of the object, which can be utilized as a reference conductivity for determination of the internal conductivity.

2.2. *Conductivity reconstruction via Kirchhoff's voltage law*

In a previous work in Kwon *et al* (2002b), the equipotential line technique was introduced by solving a first-order ordinary differential equation on the equipotential line $X(s)$,

$$\frac{\mathrm{d}X}{\mathrm{d}s}(s) = \left(\frac{\mathbf{J}(X(s))}{|\mathbf{J}(X(s))|}\right)^{\perp} \qquad \text{with} \quad X(0) = x_b \in \partial\Omega_t, \tag{9}$$

where $(\cdot)^{\perp}$ denotes the counterclockwise right angle rotation of a vector. The equipotential line technique demonstrates that a given non-vanishing current $\mathbf{J}$ and the voltage potential u on $\partial\Omega$ determine a unique isotropic conductivity by the recovery of the interior potential in Ω. Although the projected current $\mathbf{J}^P$ from the measured B_z data stably approximates the true current $\mathbf{J}$, one of the difficulties in using the equipotential line technique is due to the fact that the noise in the current propagates along the equipotential lines. The recovery of the internal conductivity using the potential by the equipotential line technique by solving (9) is, therefore, complicated and degraded by artifacts from the equipotential lines. The recovery of voltage potential using the equipotential lines is also related to noise amplification by the differentiation of the measured B_z data. Up to now, direct usage of the equipotential line method is far from practical, requiring more efficient and stable methods for the reconstruction of an internal potential.

Kirchhoff's voltage law is one of the fundamental laws which states that the total voltage around a closed loop must be zero. In this paper, we derive a direct method using Kirchhoff's voltage law to find the internal conductivity using the given current $\mathbf{J}$ in Ω. After discretization of $\overline{\Omega} = \bigcup_{i,j}^{N,N} \overline{\Omega}_{ij}$, $1 \leqslant i, j \leqslant N$, the rectangular pixel Ω_{ij} with a left-bottom point (x_i, y_j) and a right-top point (x_{i+1}, y_{j+1}), we get the following identity by $\nabla \times \nabla u = 0$ in Ω_{ij}:

$$\frac{J_x\left(\frac{x_i+x_{i+1}}{2}, y_j\right)}{\sigma\left(\frac{x_i+x_{i+1}}{2}, y_j\right)} + \frac{J_y\left(x_{i+1}, \frac{y_j+y_{j+1}}{2}\right)}{\sigma\left(x_{i+1}, \frac{y_j+y_{j+1}}{2}\right)} - \frac{J_x\left(\frac{x_i+x_{i+1}}{2}, y_{j+1}\right)}{\sigma\left(\frac{x_i+x_{i+1}}{2}, y_{j+1}\right)} - \frac{J_y\left(x_i, \frac{y_j+y_{j+1}}{2}\right)}{\sigma\left(x_i, \frac{y_j+y_{j+1}}{2}\right)} = 0, \tag{10}$$

where $J_x\left(\frac{x_i+x_{i+1}}{2}, y_j\right) = -\sigma\left(\frac{x_i+x_{i+1}}{2}, y_j\right)(u(x_{i+1}, y_j) - u(x_i, y_j))$ and the others are represented similarly. Relating with the conductivity values $\sigma\left(x_{i+1}, \frac{y_j+y_{j+1}}{2}\right)(=\sigma(p_{ij,2}))$

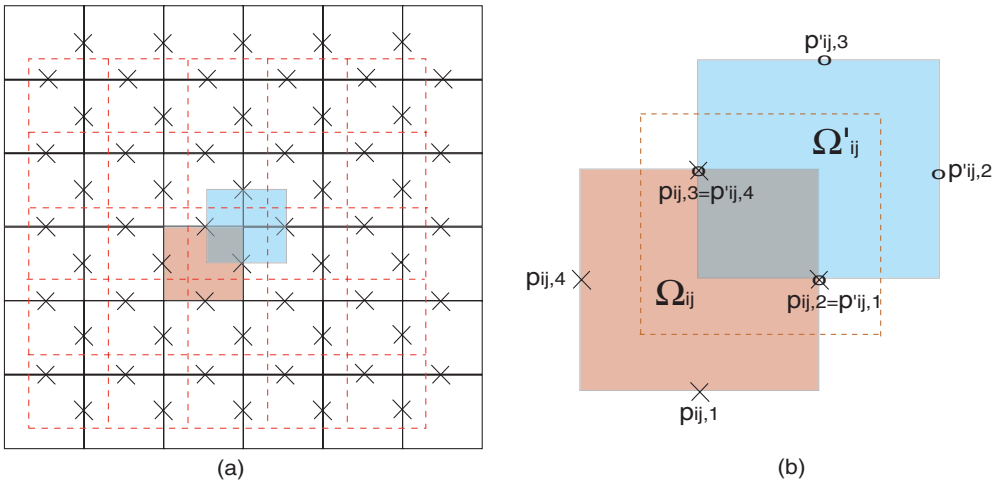

Figure 1. Schematic diagram for the dual loop with respect to a pixel.

and $\sigma\left(\frac{x_i+x_{i+1}}{2}, y_{j+1}\right)(=\sigma(p_{ij,3}))$, we can design another region Ω'_{ij} as shown in figure 1(b). Following the boundary path of Ω'_{ij}, Kirchhoff's voltage law yields

$$\frac{J_x\left(\frac{x'_i+x'_{i+1}}{2}, y'_j\right)}{\sigma\left(\frac{x'_i+x'_{i+1}}{2}, y'_j\right)} + \frac{J_y\left(x'_{i+1}, \frac{y'_j+y'_{j+1}}{2}\right)}{\sigma\left(x'_{i+1}, \frac{y'_j+y'_{j+1}}{2}\right)} - \frac{J_x\left(\frac{x'_i+x'_{i+1}}{2}, y'_{j+1}\right)}{\sigma\left(\frac{x'_i+x'_{i+1}}{2}, y'_{j+1}\right)} - \frac{J_y\left(x'_i, \frac{y'_j+y'_{j+1}}{2}\right)}{\sigma\left(x'_i, \frac{y'_j+y'_{j+1}}{2}\right)} = 0. \tag{11}$$

Identities (10) and (11) by following the two different loops $\partial\Omega_{ij}$ and $\partial\Omega'_{ij}$ share the common conductivity values $\sigma\left(x_{i+1}, \frac{y_j+y_{j+1}}{2}\right)(=\sigma(p_{ij,2})=\sigma(p'_{ij,1}))$ and $\sigma\left(\frac{x_i+x_{i+1}}{2}, y_{j+1}\right)(=\sigma(p_{ij,3})=\sigma(p'_{ij,4}))$ as shown in figure 1(b). The proposed numerical scheme is to determine conductivity values at each common region (red-dotted blocks in figure 1(a)) by the two different loops. For the determination of a representative conductivity value at the common region $\Omega_{ij} \cap \Omega'_{ij}$, the designed two loops use full information of $\mathbf{J}$ to determine the conductivity stably. For example, the y-component $J_y\left(x_{i+1}, \frac{y_j+y_{j+1}}{2}\right)$ and the x-component $J_x\left(x_{i+1}, \frac{y_j+y_{j+1}}{2}\right)$ at the point $p_{ij,2} = p'_{ij,1}$ are used simultaneously following the loops $\partial\Omega_{ij}$ and $\partial\Omega'_{ij}$, respectively. With known conductivity values near the boundary, we determine a conductivity value at the common points $\left(x_{i+1}, \frac{y_j+y_{j+1}}{2}\right)$ and $\left(\frac{x_i+x_{i+1}}{2}, y_{j+1}\right)$ of two loops as a representative conductivity value in the common pixel in figure 1(b). The representative conductivity value at the common points yields

$$\frac{J_x(p_{ij,1})}{\sigma(x_i, y_{j-1})} + \frac{J_y(p_{ij,2})}{\sigma(x_i, y_j)} - \frac{J_x(p_{ij,3})}{\sigma(x_i, y_j)} - \frac{J_y(p_{ij,4})}{\sigma(x_{i-1}, y_j)} = 0 \tag{12}$$

$$\frac{J_x(p'_{ij,1})}{\sigma(x_i, y_j)} + \frac{J_y(p'_{ij,2})}{\sigma(x_{i+1}, y_j)} - \frac{J_x(p'_{ij,3})}{\sigma(x_i, y_{j+1})} - \frac{J_y(p'_{ij,4})}{\sigma(x_i, y_j)} = 0. \tag{13}$$

There are $2(N-1)^2$ loops and Kirchhoff's voltage law provides $2(N-1)^2$ number of equations for $\overline{\Omega} = \bigcup_{i,j}^{N,N} \overline{\Omega}_{ij}$, $1 \leqslant i, j \leqslant N$, to determine the $(N-1)^2$ internal conductivity distribution. The reconstruction algorithm for the internal conductivity using the dual-loop method implicitly leads to the following overdetermined system:

$$\begin{pmatrix} \mathbf{A}_1 \\ \mathbf{A}_2 \end{pmatrix} \mathbf{s} = \begin{pmatrix} \mathbf{b}_1 \\ \mathbf{b}_2 \end{pmatrix}, \tag{14}$$

where the vector $\mathbf{s}$ consists of resistivity values, the stiff matrix $\mathbf{A}_i$, $i = 1, 2$, is the interpolated current density at the reference points $p_{ij,k}$ and $p'_{ij,k}$, $k = 1, \ldots, 4$, following the dual loop, and the load vector $\mathbf{b}_i$ consists of the known voltage difference values using the current components and the known conductivity values around the surface. The solution $\mathbf{s}$ given by the least-squares method minimizes the square sum of (14) by solving the following normal system:

$$\left(\left(\mathbf{A}_1{}^T \mathbf{A}_2{}^T \right) \begin{pmatrix} \mathbf{A}_1 \\ \mathbf{A}_2 \end{pmatrix} + \lambda \mathbf{I} \right) \mathbf{s} = \left(\mathbf{A}_1{}^T \mathbf{A}_2{}^T \right) \begin{pmatrix} \mathbf{b}_1 \\ \mathbf{b}_2 \end{pmatrix}, \tag{15}$$

where λ denotes a regularization factor and $\mathbf{A}_i{}^T$ is the transpose matrix of $\mathbf{A}_i$.

We describe the dual-loop algorithm for the conductivity reconstruction.

(i) Solve the projected current densities $\mathbf{J}^P$ by solving the two-dimensional Laplace equation (4) using the measured B_z data.

(ii) (a) Reconstruct the stiff matrix $\mathbf{A}_i, i = 1, 2$, and the load vector $\mathbf{b}_i$ in the system (14) from the reconstructed projected current $\mathbf{J}^P$ and known conductivity values around the surface.

(b) By solving the least-squares system (15), the internal conductivity σ is determined from the determined resistivity values.

An alternative way to reconstruct the internal conductivity based on Kirchhoff's voltage law is to use the one-loop method by following $\partial\Omega_{ij}$ given in figure 1. Under the assumption of the conductivity near the boundary, we can recover a representative conductivity value for each loop under consideration following a path covering the ROI:

$$\sigma(x_i, y_j) = \frac{J_y(p_{ij,2}) - J_x(p_{ij,3})}{\frac{J_y(p_{ij,4})}{\sigma(x_{i-1,y_j})} - \frac{J_x(p_{ij,1})}{\sigma(x_i, y_{j-1})}}. \tag{16}$$

Note that this procedure recovers explicitly all of the internal conductivity in a real time by starting from a known conductivity at one corner. However, the recovered conductivity values influenced by the previously recovered conductivity values also propagate noise following the current flow and may cause abrupt artifacts which influence the next determination of the conductivity value. When the denominator is close to zero, it is difficult to determine the conductivity with the one-loop method, and it is critical to take a path to alleviate such a situation by considering a different injection current.

The proposed dual-loop method compared with the one-loop explicit method determines the internal conductivity implicitly, which is independent of a path and fully uses the given internal current information, which combines all current components in the stiff matrix $\mathbf{A}_1$ and $\mathbf{A}_2$ in (14).

2.3. Experiments setup

2.3.1. Generation of two-dimensional simulated data. We constructed a two-dimensional finite-element model of a subject $\Omega = (0, 1)^2$ with 128×128 rectangular elements. We configured three objects with different isotropic conductivity values (high conductivity: 2 S m^{-1}, low conductivity: 0.5 S m^{-1}, background: 1 S m^{-1}). Current is injected from the top to the bottom. Figures 2(a)–(c) show the isotropic conductivity distribution, the potential distribution and the generated current density, respectively.

Set a Neumann flux g such that

$$g(x, y) = \begin{cases} 1, & \text{if } \left| x - \frac{1}{2} \right| \leqslant \frac{1}{10} \text{ and } y = 0 \\ -1, & \text{if } \left| x - \frac{1}{2} \right| \leqslant \frac{1}{10} \text{ and } y = 1 \\ 0, & \text{otherwise.} \end{cases}$$

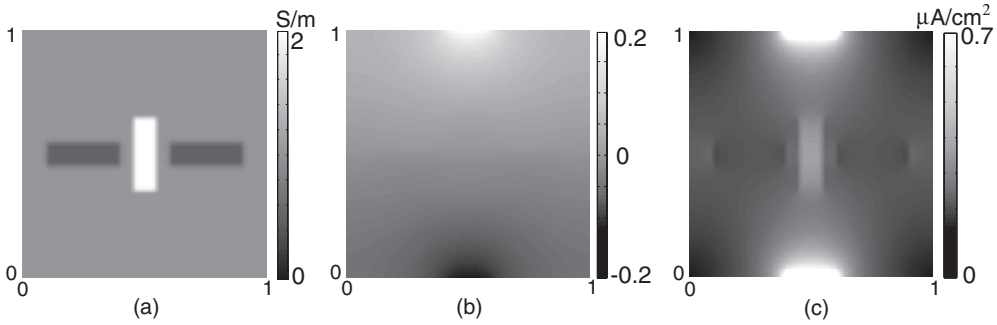

Figure 2. Two-dimensional simulation setup. (a) Conductivity distribution with high conductivity (2 S m^{-1}) and low conductivity (0.5 S m^{-1}) anomalies. (b) Voltage potential by solving the elliptic equation (1). (c) Simulated current density magnitude image.

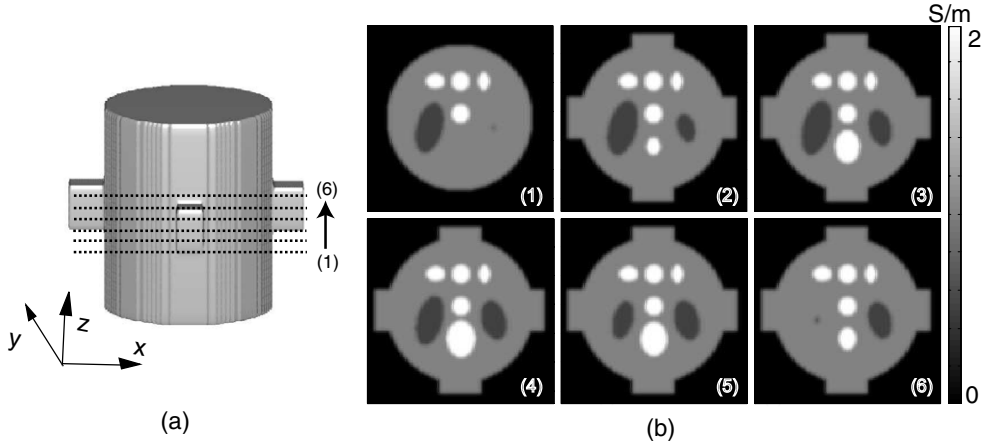

Figure 3. Three-dimensional simulation setup. (a) Three-dimensional cylindrical model. (b) Sectional conductivity distribution at the slices indicated region with high conductivity (2 S m^{-1}) and low conductivity (0.5 S m^{-1}) anomalies.

For the two-dimensional case, we recovered the conductivity distribution assuming a given current density to observe the characteristics of the proposed method.

2.3.2. Generation of three-dimensional simulated data. For a three-dimensional numerical simulation, we considered a cylindrical model with diameter 16 cm and height 12 cm as shown in figure 3(a). Two pairs of electrodes are attached around the middle of the model, through which a 10 mA current is injected. The sectional conductivity images of the target conductivity distribution from the bottom to the top with high conductivity values 2 S m^{-1}, low conductivity values 0.5 S m^{-1} and background 1 S m^{-1} are depicted in figure 3(b).

Figure 4 shows the simulated noiseless B_z data and the true current density magnitude corresponding to the sectional conductivity images in figure 3 using the three-dimensional MREIT solver (Lee *et al* 2003).

2.3.3. Generation of phantom data. For a realistic experiment, we injected current into an imaging object through a pair of surface electrodes attached on a cylindrical phantom. The

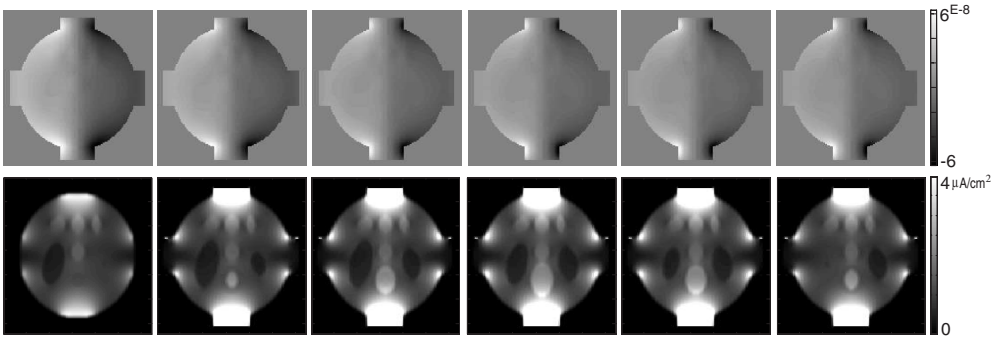

Figure 4. Three-dimensional simulation setup. The first row and the second row display the generated magnetic flux density and the current density magnitude image corresponding to the sectional conductivity images in figure 3, respectively.

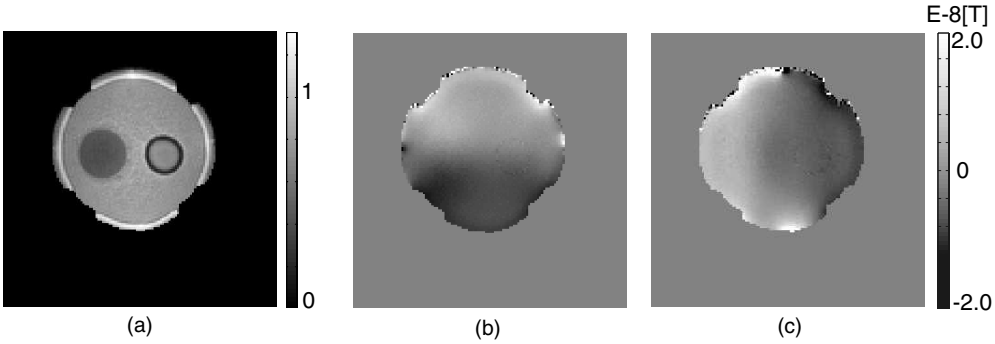

Figure 5. (a) MR magnitude image. (b) and (c) Images of the measured B_z data due to transversal and vertical injection currents at the middle imaging slice.

injected current produces an internal current density distribution influenced by the geometry of, and the conductivity distribution in, the imaging object. We measured only the z-component of the induced magnetic flux density (Muftuler *et al* 2004, Lee *et al* 2005, Birgul *et al* 2006) by using the ICNE MR pulse sequence which injected the current between the end of the first RF pulse and the end of the reading gradient (Park *et al* 2007). In this paper, we assume a static multi-slice imaging method and denote the magnetic flux density as $B_z(x, y) = B_z(x, y, z_0)$, where z_0 is the center of the selected imaging slice. The phase-encoding gradient is switched on for a brief period T_{pe} before the signal is collected during the data acquisition time duration T_s for a fixed echo time T_E.

We used a cylindrical phantom with 120 mm diameter and 120 mm height with two attached carbon-hydrogel electrodes (HUREV Co. Ltd, Korea) at the middle of the phantom. We filled the background with a saline solution (1 g l^{-1} $CuSO_4$, 2.82 g l^{-1} NaCl) to control the T_1 and T_2 decay of spin density. The conductivity value of the background is 0.9 S m^{-1}. Two cylindrical objects, where the diameters of left and right anomalies are 3.6 and 3 cm, respectively (see figure 5(a)), are filled with an agar gel (left: 1 g l^{-1} $CuSO_4$, 1.45 g l^{-1} NaCl, 15 g l^{-1} agar; right: 1 g l^{-1} $CuSO_4$, 2.1 g l^{-1} NaCl, 15 g l^{-1} agar) to create a contrast in both conductivity and spin density; the conductivity values of the left one and the right one are 1.6 and 1.2 S m^{-1}, respectively.

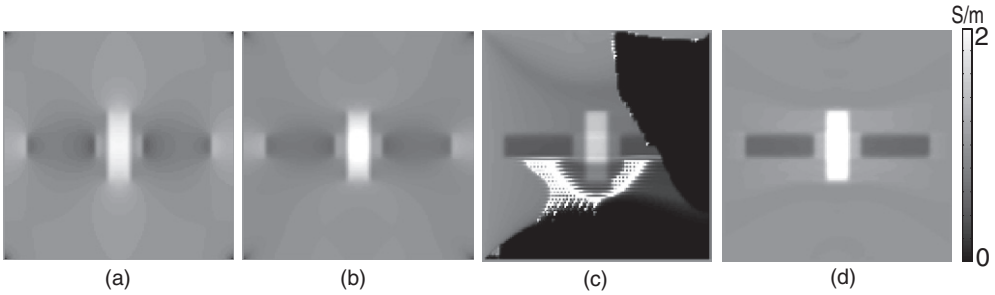

Figure 6. Two-dimensional simulation experiment results. (a) and (b) Reconstructed first and third updated conductivity images respectively using the *J*-substitution method with one injection current. (c) and (d) Reconstructed conductivity images using the one-loop method and the dual-loop method, respectively.

After positioning the phantom inside a 3.0 T MRI scanner (Magnum 3, Medinus, Korea), we collected the *k*-space MR data using the spin pulse sequence. Figures 5(b) and (c) are the measured B_z images of the phantom at the center imaged slice due to transversal and vertical injection currents, respectively.

We injected a 10 mA current and used the total current injection time duration of $T_c + T_s = 26$ ms, $T_c = 22$ ms and data acquisition time $T_s = 3.584$ ms for a fixed echo time $T_E = 30$ ms in the ICNE pulse sequence. The slice thickness was 6 mm with no slice gap, the number of axial slices was 8 at the center of the phantom and $T_R/T_E = 1000/25$ ms. The FOV was 180×180 mm^2 with the matrix size 128×128 and the NEX (number of excitation/acquisition) was 1.

3. Results

3.1. Numerical simulation results

3.1.1. Two-dimensional simulation results. To observe the relation between the one current and the conductivity, we reconstructed the conductivity with the provided internal current $\mathbf{J} = (J_x, J_y)$. Figures 6(a) and (b) show the reconstructed conductivity images σ^1 and σ^3, respectively, using the *J*-substitution algorithm with one given internal current $\mathbf{J}$ (Kwon *et al* 2002a):

$$\sigma^n(x,y) = \frac{-J_x(x,y)u_x^{n-1}(x,y) - J_y(x,y)u_y^{n-1}(x,y)}{\left(u_x^{n-1}(x,y)\right)^2 + \left(u_y^{n-1}(x,y)\right)^2}, \qquad n = 1, 2, \ldots, \tag{17}$$

where u^n is the nth updated potential by solving (1) with the conductivity distribution of σ^{n-1}. The reconstructed σ^1 shows that the edge of the anomaly D with a low conductivity value 0.5 S m^{-1} was not clear because the current $\mathbf{J}$ was relatively parallel to the outer normal vector of ∂D, and therefore the third updated σ^3, which was influenced by the previous updated conductivity, also could not distinguish the edge of the anomaly clearly even if the conductivity value was fixed near the boundary of Ω.

Figure 6(c) shows the reconstructed conductivity using the one-loop method starting from left-top of Ω. We directly implemented the method, and the reconstructed conductivity was severely deteriorated by a pixel including abruptly changed current flow. Although, of course, it may be possible to generate a better reconstructed image than the reconstructed one in figure 6(c) by a more careful management of the current flow and noise , it is inherently difficult to reflect a local change of the current flow and to manage the noise effect following

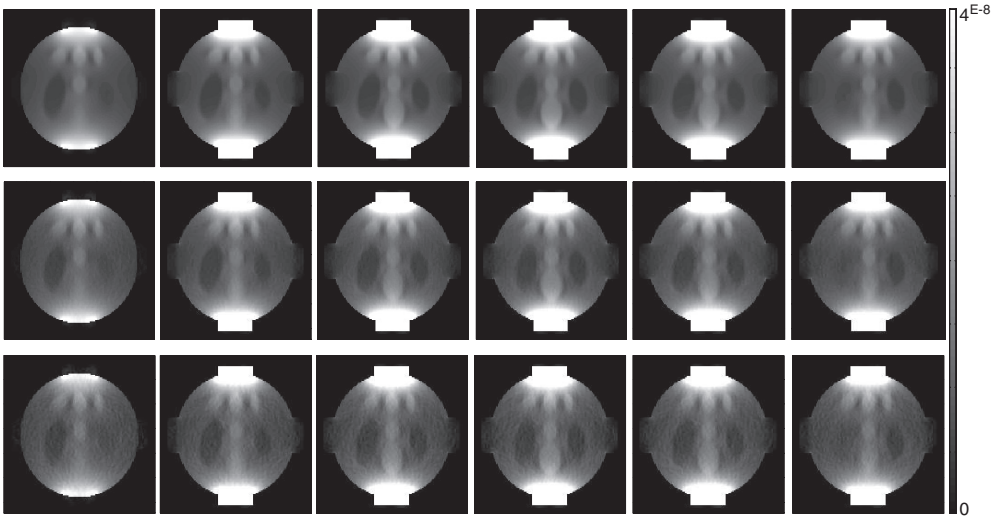

Figure 7. Three-dimensional simulation results. The first, second and third rows show the reconstructed projected current by adding random noise, SNR $= \infty$, 100, 50, to B_z data at the sectional slices in figure 3, respectively.

the current flow by the one-loop method which reconstructs the conductivity pixel-by-pixel using a pathway (Kwon *et al* 2002b, Ozdemir *et al* 2004).

The reconstructed conductivity using the proposed dual-loop method is displayed in figure 6(d). We took a dual loop as in figure 1, which is induced to a global system $\mathbf{A}^T Ax = A^T b$, $\mathbf{A} = \begin{pmatrix} \mathbf{A}_1 \\ \mathbf{A}_2 \end{pmatrix}$ and $\mathbf{b} = \begin{pmatrix} \mathbf{b}_1 \\ \mathbf{b}_2 \end{pmatrix}$, combining Kirchhoff's law and the resistivity directly. To estimate that the condition number of $\mathbf{A}^T A$ was 183 804.4, we used the power method and inverse power method for the largest and the smallest eigenvalues, respectively. The equipped over-determined matrix system was solved by a conventional sparse matrix conjugate gradient solver.

3.1.2. Three-dimensional simulation results. We depicted the projected current $\mathbf{J}^P = \mathbf{J}^0 + \left(\frac{\partial \beta}{\partial y}, -\frac{\partial \beta}{\partial x}, 0\right)$ by solving (4) in figure 7 at the middle slices of the cylindrical model in figure 3(a). The recovered projected current $\mathbf{J}^P$ shows considerable information of the true current $\mathbf{J}$ even if the true current is not exactly two-dimensional current.

Since the noise standard deviation s_{B_z} of the measured B_z is inversely proportional to the width of injected current, T_c, and the SNR of the MR magnitude image Υ (Scott *et al* 1992) as

$$s_{B_z} = \frac{1}{2\gamma T_c \Upsilon}, \tag{18}$$

to test the tolerance of the projected current to artificially generated noise, we added random noise by following $\frac{s_{B_z}\Upsilon}{\mathrm{SNR}}$, where $\gamma = 26.75 \times 10^7$ rad T^{-1} s^{-1} denoted the gyromagnetic ratio of hydrogen and the current injection time $T_c = 50$ ms. The second and third rows in figure 7 show the reconstructed projected current by adding random noise, SNR $= 100$ and 50 cases, to B_z data at the sectional slices in figure 3, respectively.

With the projected current $\mathbf{J}^P$, we recovered the conductivity images at the middle slices in figure 3. To prove the performance of the dual-loop algorithm, we used two internal projected currents by vertical and horizontal injection currents which induced the doubled

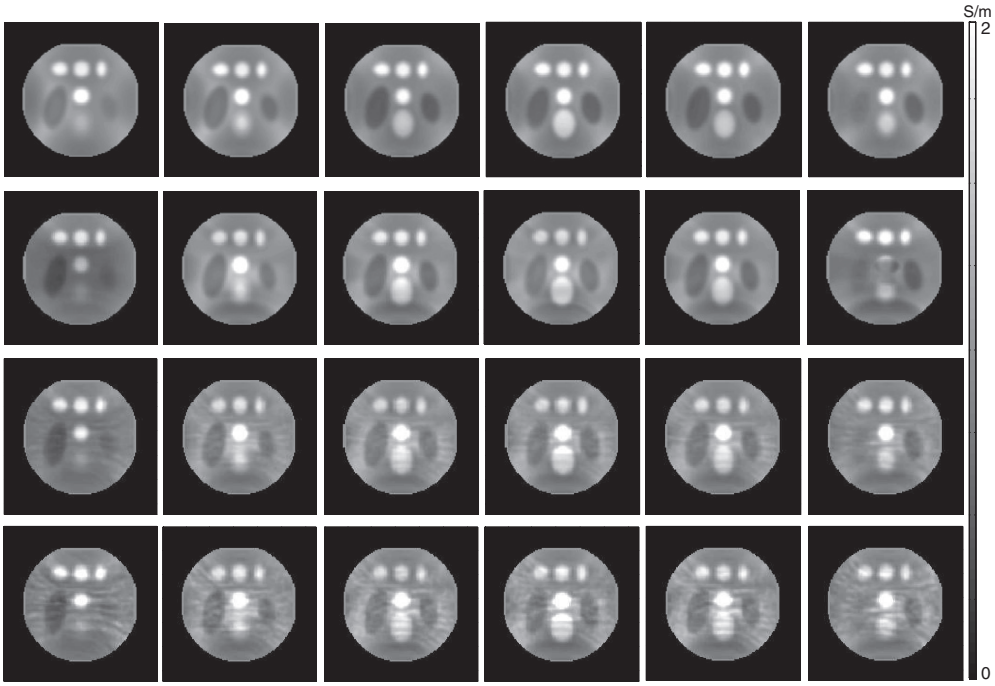

Figure 8. Three-dimensional simulation results at the middle slices in figure 3. The first row shows the reconstructed conductivity images using two projected currents $\mathbf{J}^{P,1}$ and $\mathbf{J}^{P,2}$. The second, the third, and the fourth row show the reconstructed conductivity images using the dual-loop method with one current $\mathbf{J}^P$ corresponding to the noise level SNR $= \infty$, 100 and 50, respectively.

over-determined system of (14). The first row in figure 8 shows the reconstructed conductivity images using two projected currents. The second, the third, and the fourth row show the reconstructed conductivity images using the dual-loop method with one projected current $\mathbf{J}^P$ corresponding to the vertically injected current and the noise level SNR $= \infty$, 100 and 50, respectively. For the noise level SNR $= \infty$, the estimated condition numbers of the overdetermined system $\mathbf{A}^T Ax = A^T b$ for the vertically injected current were 87 607.4, 208 594.7, 288 736.9, 304 122.3 and 284 449.9 corresponding to the slices from $\mathcal{N}_{C-2}$ to $\mathcal{N}_{C+2}$, respectively.

For each noise level SNR $= \infty, 100, 50$, the relative errors $E_r(\sigma^r)$ between the reconstructed conductivity and the true σ defined by

$$E_r(\sigma^r) := \frac{\|\sigma^r - \sigma\|_{\mathcal{N}_{C+k}}}{\|\sigma\|_{\mathcal{N}_{C+k}}}, \qquad k = -2, -1, \ldots, 2, \tag{19}$$

are shown in table 1, where $\|\cdot\|$ is the L^2-norm and $\mathcal{N}_C$ denotes the middle imaging slice.

3.1.3. Phantom experiment results. Figures 9(a) and (b) ((c) and (d)) show the J_x^P and J_y^P components of the reconstructed projected current $\mathbf{J}^P = \mathbf{J}^0 + \mathbf{J}^*$ corresponding to the measured B_z data in figure 5(b)((c)), respectively. Using the projected current $\mathbf{J}^P = \left(J_x^0 + \frac{\partial \beta}{\partial y}, J_y^0 - \frac{\partial \beta}{\partial x}, J_z^0\right)$, we reconstructed the internal conductivity distribution σ to prove the proposed algorithm.

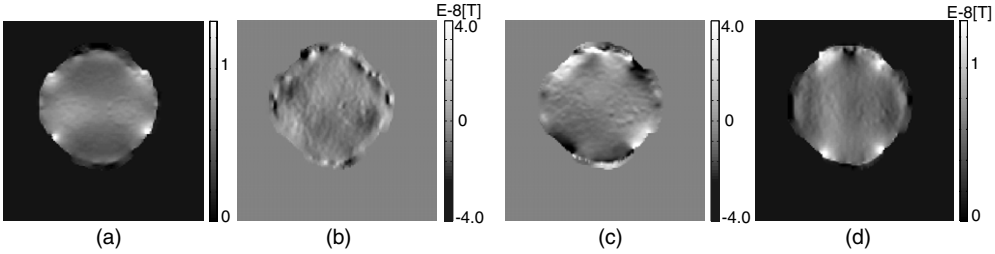

Figure 9. Phantom experiment results. (a) and (b) ((c) and (d)) Recovered current component J_x^P and J_y^P corresponding to the measured magnetic flux density data B_z in figure 5(b) ((c)), respectively.

Table 1. Relative L^2-error $E_r(\sigma^r)$ for the dual-loop method corresponding to the reconstructed conductivities in figure 8 where $\mathcal{N}_C$ denotes the middle slice.

	$E_r[\mathbf{J}^{P,1}, \mathbf{J}^{P,2}, \infty]$	$E_r[\mathbf{J}^P, \infty]$	$E_r[\mathbf{J}^P, 100]$	$E_r[\mathbf{J}^P, 50]$
$\mathcal{N}_{C-2}$	0.1709	0.2739	0.1859	0.1879
$\mathcal{N}_{C-1}$	0.1718	0.1751	0.1825	0.2137
$\mathcal{N}_C$	0.1669	0.1927	0.1865	0.2258
$\mathcal{N}_{C+1}$	0.1740	0.2024	0.2247	0.2356
$\mathcal{N}_{C+2}$	0.1873	0.2318	0.2346	0.2256

The magnitude image depending on the T_2 (or T_2^*) decay in figure 5(a) included a defected region $\mathcal{D}$ around the right cylindrical anomaly. From the analysis by Scott *et al* (1992) and Sadleir *et al* (2005), the noise standard deviation s_{B_z} of the measured B_z is inversely proportional to the current pulse width T_c and the intensity of the MR magnitude image Υ as

$$s_{B_z} = \frac{1}{2\gamma T_c \Upsilon}. \tag{20}$$

Since the intensity of the magnitude in $\mathcal{D}$ was weak, the measured B_z data in figure 5(b) and (c) were also defected in the region $\mathcal{D}$.

To reconstruct the conductivity, we used the transversal J-substitution algorithm (Nam *et al* 2007), which directly used two independent currents. Figure 10(a) shows the reconstructed conductivity image using two measured B_z data simultaneously, corresponding to figures 5(b) and (c). We made an overdetermined system (14) and used a conventional conjugate gradient solver to obtain the internal conductivity distribution. The estimated condition number of the overdetermined system $\mathbf{A}^T Ax = A^T b$ was 68 611.5. Comparing the reconstructed conductivity using two measured B_z data generated by transversal and vertical injected currents, figure 10(b) shows the recovered conductivity image using the proposed dual path method with the measured B_z data by the transversal injection current. Image (c) shows the recovered conductivity by using the measured B_z data by the vertically injected current. From figures 10(b) and (c), we observed that the dual-loop method stably recovered the conductivity and provided distinguishable contrast of conductivity.

4. Discussion

There are two main steps to apply the dual-loop method to reconstruct the conductivity distribution using one injection current: the first step is to recover the internal current on the

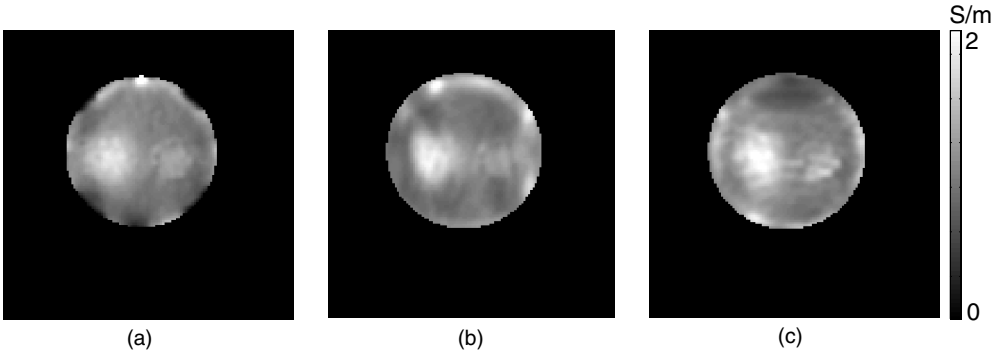

Figure 10. Phantom experiment results. (a) Recovered conductivity image using the transversal *J*-substitution algorithm with the two measured B_z data by horizontal and vertical injection currents. (b) and (c) Recovered conductivity images using the proposed dual-loop method with the measured B_z data by transversal and vertical injection currents, respectively.

imaging slice from the measured B_z data and the second step is to recover the conductivity distribution from the recovered single internal current. The projected current, $\mathbf{J}^P = \mathbf{J}^0 + \mathbf{J}^*$, obtained by solving the two-dimensional harmonic equation (4) has provided a quite feasible internal current in many numerical and phantom experiments when the z-component of $\mathbf{J}$ is similar to the z-component of $\mathbf{J}^0$. A critical step is to extract the conductivity information from the one internal current. Since MREIT imaging techniques to visualize the conductivity have suffered from the measured noise in B_z, if experimental environments allow a sufficient scanning time using plural independent injection currents, the use of plural measured B_z data may provide a better conductivity image by compensating each other.

In section 2.2, we assumed known conductivity values near the surface to derive the proposed dual-loop method. Although the one-loop method is very unstable to recover the whole conductivity distribution in Ω, theoretically, it needs only one reference conductivity value at a starting pixel to determine conductivity values depending on a path covering Ω. Considering the advantage of the one-loop method, the assumed known conductivity values near the surface can be partially recovered by the one-loop method, where the denominator $\frac{J_y(p_{ij,4})}{\sigma(x_{i-1,y_j})} - \frac{J_x(p_{ij,1})}{\sigma(x_i,y_{j-1})}$ in (16) provides a sufficient signal.

However, using one measured B_z data by one injection current is strongly recommended in functional MREIT which is one of the promising works in MREIT or in some practical situations such as DBS and organs near the heart. We focused on reconstructing the conductivity using one measured B_z data with the reference conductivity values near the boundary. In spite of numerous potential clinical applications of MREIT as discussed in Woo and Seo (2008), scaled conductivity imaging of the human leg was the first human imaging experiment in MREIT (Kim *et al* 2009). It is still difficult to perform *in vivo* human experiments due to a long scan time and high injection current. In the case of brain imaging in MREIT, postmortem and *in vivo* animal imaging experiments (Kim *et al* 2008, 2009) have reconstructed the conductivity distribution in the brain region, and the measured B_z were seriously defected in other local regions where phase signals and MR magnitude image data are small. Defected situations may occur in local regions belonging to lungs, liver, head and bones in which typical MR images have a very low SNR. Although the current is shunted around the scalp and limits an amount of current into the brain, recent experiments in MREIT reports that the flexible carbon-hydrogel electrodes with a large surface area can inject more current without producing a painful sensation (9 mA current for the human leg

case). For partial conductivity information near the boundary, it seems possible that the usage of the measured B_z data near the boundary with known conductivity values can determine the absolute conductivity value in the brain using the dual-loop method. The development of a local approach algorithm by generalizing the projected current and the dual-loop method for a defected B_z data will be valuable in MREIT.

In the case of DBS using one injection current, it is difficult to apply the conventional techniques in MREIT to visualize the internal conductivity distribution. The proposed dual-loop method using the measured B_z corresponding to one injection current may provide a contrast conductivity image and/or the current flow around the DBS electrode.

The projected current $\mathbf{J}^P$ is recovered by the reconstruction of $\tilde{\nabla}\beta$ in (4), and the noise level of $\mathbf{J}^P$ suppresses the noise amplification by the double differentiation of B_z by solving the elliptic partial differential equation. For the equipotential line technique (Kwon *et al* 2002b), the recovery of a potential using the equipotential line from a given current $\mathbf{J}$ also includes noise accumulation along the equipotential lines, and the recovery of the conductivity from the recovered potential also amplifies the noise. In this sense, even the one-loop method directly applying Kirchhoff's voltage law may be more advantageous than the equipotential method. The noise amplification by solving the over-determined system in (14) depends on the noise level of the stiff matrices $\mathcal{A}_\infty$ and $\mathcal{A}_\in$, composed of $\mathbf{J}^P$, and the condition number of the normal matrix in (15).

Since the projected current $\mathbf{J}^P = \mathbf{J}^0 + \mathbf{J}^*$ can be recovered when the conductivity is anisotropic, it will be very useful to investigate the relation between the projected current and the more general anisotropic conductivity. One promising work based on one measured B_z by one injection current is to develop a reconstruction algorithm for the anisotropic conductivity. Diffusion tensor imaging is a practical technique that enables us to investigate the anisotropy of nerve fibers in the brain of a human. We believe that MREIT may be a possible approach to obtain anisotropic properties in the brain and to investigate the associated clinical usage. Our future work will include the development of an efficient and stable algorithm for anisotropic conductivity imaging.

5. Conclusion

In this paper, we propose a new algorithm, the dual-loop method, to reconstruct the isotropic conductivity distribution in the electrically conductive object with the measured magnetic flux density B_z by only one injection current. To reconstruct the conductivity, first we determine the projected current $\mathbf{J}^P$ from the measured B_z which is a good approximation of the true current $\mathbf{J}$. By investigating the relations between the projected current flow and the interior potential, we designed two loops around each pixel from which to reconstruct an implicit over-determined matrix system for the determination of the internal conductivity. Results from numerical simulations show that the dual-loop algorithm stably determined the conductivity distribution in the imaging slice. We compared the reconstructed conductivities using one injection current and two independent injection currents with agarose gel phantom experiments.

Acknowledgments

O I Kwon was supported by the Basic Science Research Program through the National Research Foundation of Korea (NRF) funded by the Ministry of Education, Science and Technology (2010-0022398). E J Woo was supported by the SRC/ERC program (R11-2002-103) of MEST/NRF. M G Lee and Y J Kim were supported by the National Research Foundation of Korea (2009-0077987).

References

Birgul O, Eyuboglu B M and Ider Y Z 2003 Current constrained voltage scaled reconstruction (CCVSR) algorithm for MR-EIT and its performance with different probing current patterns *Phys. Med. Biol.* **48** 653–71

Birgul O, Hamamura M, Muftuler L and Nalcioglu O 2006 Contrast and spatial resolution in MREIT using low amplitude current *Phys. Med. Biol.* **51** 5035–49

Cogiamanian F, Vergari M, Pulecchi F, Marceglia S and Priori A 2008 Effect of spinal transcutaneous direct current stimulation on somatosensory evoked potentials in humans *Clin. Neurophysiol.* **119** 2636–40

Gilbarg D and Trudinger N S 1983 *Elliptic Partial Differential Equations of Second Order* (Berlin: Springer)

Gao N, Zhu S A and He B A 2006 New magnetic resonance electrical impedance tomography (MREIT) algorithm: the RSM-MREIT algorithm with applications to estimation of human head conductivity *Phys. Med. Biol.* **51** 3067–83

Hamamura M, Muftuler L, Birgul O and Nalcioglu O 2006 Measurement of ion diffusion using magnetic resonance electrical impedance tomography *Phys. Med. Biol.* **51** 2753–62

Ider Y Z and Birgul O 1998 Use of the magnetic field generated by the internal distribution of injected currents for electrical impedance tomography (MR-EIT) *Elektrik* **6** 215–25

Ider Y Z and Onart S 2004 Algebraic reconstruction for 3D MR-EIT using one component of magnetic flux density *Physiol. Meas.* **25** 281–94

Ider Y Z, Onart S and Lionheart W R B 2003 Uniqueness and reconstruction in magnetic resonance-electrical impedance tomography(MR-EIT) *Physiol. Meas.* **24** 591–604

Joy M L G, Scott G C and Henkelman R M 1989 *In vivo* detection of applied electric currents by magnetic resonance imaging *Magn. Reson. Imaging* **7** 89–94

Kim H J, Kim Y T, Minhas A S, Jeong W C, Woo E J, Seo J K and Kwon O J 2009 *In vivo* high-resolution conductivity imaging of the human leg using MREIT: the first human experiment *IEEE Trans. Med. Imaging* **28** 1681–7

Kim Y J, Kwon O, Seo J K and Woo E J 2003 Uniqueness and convergence of conductivity image reconstruction in magnetic resonance electrical impedance tomography *Inverse Problems* **19** 1213–25

Kim H J *et al* 2008 *In vivo* electrical conductivity imaging of a canine brain using a 3 T MREIT system *Physiol. Meas.* **29** 1145–55

Kringelbach M, Jenkinson N, Owen S and Aziz T 2007 Translational principles of deep brain stimulation *Nat. Rev. Neurosci.* **8** 623–35

Kwon O, Lee J Y and Yoon J R 2002b Equipotential line method for magnetic resonance electrical impedance tomography (MREIT) *Inverse Problems* **18** 1089–100

Kwon O, Woo E J, Yoon J R and Seo J K 2002a Magnetic resonance electrical impedance tomography (MREIT): simulation study of J-substitution algorithm *IEEE Trans. Biomed. Eng.* **48** 160–7

Lee B I, Lee S H, Kim T S, Kwon O, Woo E J and Seo J K 2005 Harmonic decomposition in PDE-based denoising technique for magnetic resonance electrical impedance tomography *IEEE Trans. Biomed. Eng.* **52** 1912–20

Lee B I, Oh S H, Woo E J, Lee S Y, Cho M H, Kwon O, Seo J K, Lee J Y and Baek W S 2003 Three-dimensional forward solver and its performance analysis in magnetic resonance electrical impedance tomography (MREIT) using recessed electrodes *Phys. Med. Biol.* **48** 1971–86

Lee J Y 2004 A reconstruction formula and uniqueness of conductivity in MREIT using two internal current distributions *Inverse Problems* **20** 847–58

Muftuler L, Hamamura M, Birgul O and Nalcioglu O 2004 Resolution and contrast in magnetic resonance electrical impedance tomography (MREIT) and its application to cancer imaging *Tech. Cancer Res. Treat.* **3** 599–609

Nam H S, Lee B I, Choi J, Park C and Kwon O 2007 Conductivity imaging with low level current injection using transversal J-substitution algorithm in MREIT *Phys. Med. Biol.* **52** 6717–30

Oh S H, Lee B I, Park T S, Lee S Y, Woo E J, Cho M H, Kwon O and Seo J K 2004 Magnetic resonance electrical impedance tomography at 3 Tesla field strength *Magn. Reson. Med.* **51** 1292–6

Oh S H, Lee B I, Woo E J, Lee S Y, Cho M H, Kwon O and Seo J K 2003 Conductivity and current density image reconstruction using harmonic B_z algorithm in magnetic resonance electrical impedance tomography *Phys. Med. Biol.* **48** 3101–16

Oh S H, Lee B I, Woo E J, Lee S Y, Kim T S, Kwon O and Seo J K 2005 Electrical conductivity images of biological tissue phantoms in MREIT *Physiol. Meas.* **26** S279–88

Ozdemir M, Eyuboglu B M and Ozbek O 2004 Equipotential projection-based magnetic resonance electrical impedance tomography and experimental realization *Phys. Med. Biol.* **49** 4765–83

Park C, Lee B I and Kwon O 2007 Analysis of recoverable current from one component of magnetic flux density in MREIT *Phys. Med. Biol.* **52** 3001–13

Sadleir R *et al* 2005 Noise analysis in MREIT at 3 and 11 Tesla field strength *Physiol. Meas.* **26** 875–84

Scott G C, Joy M L G, Armstrong R L and Henkelman R M 1991 Measurement of nonuniform current density by magnetic resonance *IEEE Trans. Med. Imaging* **10** 362–74

Scott G C, Joy M L G, Armstrong R L and Hankelman R M 1992 Sensitivity of magnetic resonance current density imaging *J. Magn. Reson.* **97** 235–54

Seo J K, Yoon J R, Woo E J and Kwon O 2003 Reconstruction of conductivity and current density images using only one component of magnetic field measurements *IEEE Trans. Biomed. Eng.* **50** 1121–4

Woo E J and Seo J K 2008 Magnetic resonance electrical impedance tomography (MREIT) for high-resolution conductivity imaging *Physiol. Meas.* **29** R1–26